1 **China Wildfire Emission (ChinaWED v1) for the period 2012-2022**

2

3 Zhengyang Lin[a], Ling Huang[a], Hanqin Tian[b], Anping Chen[c], Xuhui Wang[a*]

4

5 a. Institute of Carbon Neutrality, Sino-French Institute of Earth System Sciences,
6 College of Urban and Environmental Sciences, Peking University, Beijing, China
7 b. Center for Earth System Science and Global Sustainability, Schiller Institute for
8 Integrated Science and Society, Department of Earth and Environmental Sciences,
9 Boston College, Chestnut Hill, MA, USA
10 c. Department of Biology and Graduate Degree Program in Ecology, Colorado State
11 University, Fort Collins, USA
12 *Correspondence to*: Xuhui Wang(xuhui.wang@pku.edu.cn)

13

14

15 ## Abstract

16   During the past decades, wildfires have undergone rapid changes while both the
17 extent of fire activities and the resulting greenhouse gas (GHG) emissions from
18 wildfires in China remain inadequately quantified. To explore national wildfire-induced
19 emissions, we employed satellite-based data on burned vegetation to generate the
20 China Wildfire Emission Dataset (ChinaWED). This dataset is constructed at monthly
21 and kilometer scale under a consistent and quantifiable calculation framework,
22 providing an average annual estimates of wildfire-induced GHG emissions of 78.13 ±
23 22.46 Tg CO_2, 279.47 ± 82.01 Gg CH_4, and 6.26 ± 1.67 Gg N_2O for the past decade.
24 We observed significant decreases in both wildfire occurrences and emissions within
25 forests and grasslands. This trend, however, is counteracted by increasing agricultural
26 fires, which constitute the primary type accounting for at least half of the national total
27 fire emissions. The seasonal cycle of wildfire GHG emissions show an evident apex
28 occurring during the transition from mid-spring to early-summer. At the regional scale,
29 Northeast, Southwest and East China emerge as hotspots for wildfire-induced
30 emissions. Our study offers new insights into understanding China's wildfire dynamics
31 and provides a detailed regional model for the wildfire greenhouse gas emissions over
32 China.

33

1. Introduction

34

35 Wildfires exert a substantial impact on landscape vegetation while influencing the
36 biogeochemical cycle through the emissions of greenhouse gases (GHG) (Bauters et
37 al., 2021; Guo et al., 2024; Rodríguez Vásquez et al., 2021). Approximately 2.1×10^{15}
38 grams (Petagrams, Pg) of carbon were emitted globally through biomass burning,
39 representing about 22% of all fossil fuel emissions in 2021 (Friedlingstein et al., 2022;
40 van Wees et al., 2022; van der Werf et al., 2017). It constitutes a crucial component of
41 the global and regional GHG budget (carbon dioxide (CO_2), methane (CH_4) and nitrous
42 oxide (N_2O)), which is of particular concern giving 120 countries have pledged to
43 achieve net zero GHG emissions. China, in particular, announced and initiated long-
44 term climate plans, aiming for carbon peaking by 2030 and carbon neutrality by 2060
45 (Liu et al., 2022). Additionally, over the past decade in China, climate-driven fire
46 weather, expanding vegetation-based fuel loadings, and anthropogenic activities have
47 led to rapidly changing fire dynamics (Wang et al., 2023a; Wiedinmyer et al., 2023;
48 Ying et al., 2018). To address the challenge and achieve the goals, one key step is to
49 establish a national scale dataset that reflects the recent wildfire emission dynamics
50 and contributes to the domestic GHG budget (Friedlingstein et al., 2022).

51 Currently, there have been different studies working on the estimates of China
52 wildfire emissions including contributions from some global products. One of the most
53 widely-used approaches take the product of emission factors, fuel loadings, burned
54 area and combustion efficiency as the estimate of emissions. It should be noted that
55 the limitations stem from various aspects during the calculation steps. For example,
56 these studies may use the universal parameters (e.g., land cover types, emission
57 factors) that do not match with characteristics of local fuels and further estimates (van
58 Wees et al., 2022; Wiedinmyer et al., 2023). Uncertainty also arises from estimates of
59 burned area due to the remote sensing-based fire datasets with different emphasis
60 (e.g., active fire product and burned area product) (Chen et al., 2020; Giglio et al., 2018;
61 Schroeder et al., 2014). Some other research focused on agricultural fire emissions
62 adopted traditional "crop-yield-based approaches" (CYBAs), primarily relying on
63 provincial statistical data and field-reported measurements such as crop production
64 and estimates of burned crop residues (Hong et al., 2023; Li et al., 2016). These parts
65 are hard to verify and can only be measured within administrative boundaries. In
66 addition, the estimates from CYBAs typically have relatively long updating cycles, often
67 on a yearly scale. These approaches form the fundamental framework of emission
68 estimates, yet various input parameters were incorporated and the emissions of GHGs
69 may not be consistent even within products.

70 Here, we present the China Wildfire Emission Dataset (ChinaWED v1) for the
71 period from 2012 to 2022 at monthly and kilometer scale. We focused on the limitations
72 existing in current studies and products and refined the estimates of calculation
73 components. Emission factors that are specifically suited for evaluating wildfire
74 emission in China retrieved from previous studies conducted domestically and in
75 neighboring countries were collected. Previous studies have reported a majority of
76 wildfire occurrences in croplands, highlighting the need for improved burned area

77 estimates that incorporate small-size fire activities (Ying et al., 2021; Zhang et al.,
78 2015). The newly developed product is easily to update with only one-month to two-
79 months lag and provide consistent results for all three GHGs under same calculation
80 framework. With the support of this ChinaWED product, we can also capture and
81 explore the magnitude, patterns, trends and drivers of the wildfire occurrences and the
82 wildfire-induced emissions in China within the past decade.
83

2. Methods

2.1 Emission estimation

86 In this study, we adopted the wildfire emissions estimation method based on the
87 combination of four components: burned area, fuel load, emission factor and
88 combustion completeness, calculated by the following equation:

$$E_{i,x,t} = \sum_{j}^{n} BA_{t,x} \times FL_x \times EF_{i,j} \times CC_{x,j} \qquad (1)$$

90 where the subscript i represents specific emission types, j represents different
91 vegetated cover types, x and t stand for spatial and temporal information; $E_{i,x,t}$ is
92 hence the estimated amount of emission type i in location x and month t; $BA_{t,x}$ is
93 the total aggregated burned area derived from multisource of satellite-based products
94 in location x and month t; FL_x is fuel load in location x; $EF_{i,j}$ is emission factor of
95 specific emission type i for vegetated cover type j; $CC_{x,j}$ is defined as combustion
96 completeness in location x for vegetated cover type j.
97

2.2 Burned area calculation

99 Satellite-based thermal anomalies include burned area and active fire products,
100 equipping researchers with the capability to observe these distinctive signatures
101 across extensive spatial and temporal ranges. Burned areas are determined by
102 analyzing the disparities in visible and near-infrared channels between pre- and post-
103 fire satellite images. One of the most common limitations in burned area products is
104 the exclusion of small-sized or smoldering fires. In contrast, active fire detection is
105 capable of sensing these fires benefitting from the use of the thermal-sensitive mid-
106 infrared channel. Here we use MODIS burned area product and achieved FIRMS
107 VIIRS S-NPP active fire records   as the main input datasets (Giglio et al., 2018;
108 Schroeder et al., 2014).
109 MCD64A1 provides burned area classification at 500 m spatial resolution and
110 monthly temporal resolution. VIIRS S-NPP provides daily active fire detection at 375
111 m spatial resolution. Given active fire detection's capability to identify fires occupying
112 5% or less of a pixel, the S-NPP active fire records can provide more detailed
113 information, particularly in regions like China where numerous crop residue burnings
114 occur. Current models and studies counted the active fire points located outside
115 existed burned area directly as the supplementary sources for the fire activities. To
116 avoid the potential excessive measurement, a reanalysis system combining both

117 burned area and active fire was designed and demonstrated in Fig S1. We
118 reconstructed the external burned area derived with circular kernels centered at those
119 active fire records. The aggregated burned area is calculated as below:

120
$$BA_{t,x} = BA_{main(t,x)} + \sum_{m}^{n} AF_{sf(t,x,m)} \qquad (2)$$

121   where the subscript and left part of the equation is same with that in equation (1);
122 $BA_{main(t,x)}$ represents the burned area cells in location x and month t; the sum of
123 $AF_{sf(t,x,m)}$ represents potential burned area determined through the counting of
124 decomposed small pixels from circular kernels centered at those active fire records
125 (Fig. S3 and Fig. S4).
126   Additionally, we incorporated an independent inventory of fixed-location heat
127 sources. This inventory is featured by continuously operating heat-source objects and
128 spatiotemporal-aggregation characteristics in thermal anomalies. It encompasses
129 heat-source objects including active volcanos, industrial heat sources (e.g., coal-
130 related plants, nonmental mineral producing, ferrous metal related plants) (Liu et al.,
131 2018). We utilized this inventory as a filter to exclude "burned areas" pixels that are
132 not caused by wildfires. Finally, the processed burned area results were resampled to
133 1 km spatial resolution to match the fuel load and land cover mapping. In general,
134 nearly three quarters (76.2%) of the total burned area is derived directly from the
135 MCD64 burned area product, while 24.5% is supplemented by information from VIIRS
136 S-NPP 375 m active fire records Through the incorporation of an independent fixed
137 heat source dataset, we were able to filter out 0.7% of the burned area.
138

139 **2.3 Calculation of other components**

140   Prior studies integrated upscaled systematic field investigations and regional or
141 national censuses to map the fuel load. Recent results showed that AGB can serve as
142 a proxy observation, enabling indirect estimations of dry matter. Remotely sensed
143 biomass carbon density maps aiming at limited vegetation types have been widely
144 used. Here we used the newly developed 300 m spatial resolution dataset from Spawn
145 et al. that incorporates multisource previously presented biomass map and harmonizes
146 AGB from different vegetation types (Noon et al., 2022; Spawn et al., 2020).
147   We used land cover product from the ESA Climate Change Initiative to describe
148 the different vegetation types (Li et al., 2018). This product has identical spatial
149 resolution to this harmonized AGB dataset. We further aggerated the initial 37 classes
150 into three major vegetated categories, namely forests, herbaceous and cropland. To
151 refine the estimation of crop residue burning, several independent datasets of high-
152 resolution crop type mapping are utilized as well. These dataset contain spatial
153 distribution of double season paddy rice (Pan et al., 2021), single season rice (Shen
154 et al., 2023), maize (Shen et al., 2022), winter wheat (Dong et al., 2020) and sugarcane
155 (Zheng et al., 2022) with 10 m or 20 m spatial resolution.
156   It should be noted that the resolution of all these above datasets were downscaled
157 to 1 km. AGB was calculated by summing all pixels, land cover was determined based
158 on the mode value of vegetated categories, and detailed crop types were identified by

159   counting classified pixels. AGB provided consistent and seamless estimations of
160   biomass carbon density globally for the fixed year 2010. Land cover data were
161   computed from 2001 to 2020, while crop type mapping was primarily calculated
162   between 2017 and 2020. We utilize annual land cover data associated with the burned
163   area for the corresponding year (mapping the burned area in 2020 for the period from
164   2020 to 2022). For distinct crop types, we specifically employ the results obtained
165   during their respective growing seasons, coupled with the monthly burned area data.
166   The averaged multiyear crop type mapping was harmonized into land cover data where
167   agricultural land use pixels were present.

168   Different previous studies applied constant thresholds which is considered a major
169   bias in emission estimation (Zhang et al., 2008). We adopted a method based on the
170   combination of land cover types and fraction of burned (FB) assigned as a function of
171   tree cover (Wiedinmyer et al., 2023; Wu et al., 2018; Zhang et al., 2011). Agricultural
172   land use was set to fixed combustion completeness value to 0.93. Herbaceous had
173   similar high CC values defined by the fraction of tree coverage while forests had much
174   lower CC values. The detail values are listed in Table S.1 .

175   Emission factors for different vegetation and emission types were summarized in
176   Table S.2. Apart from the studies that introducing global fire emissions, we selected
177   publications that focused on affected burned areas in China and neighboring countries.
178   Detailed emission factors of different crop types were one of the primary objectives
179   and used in this study to help improve our burned area-based emission estimation.
180   Forests were divided into tropical, temperate and boreal types, identified by the
181   updated digital Köppen–Geiger world map of climatic classification (Beck et al., 2018).
182

3. Results

3.1 Characteristics of China wildfires and emissions

185   ChinaWED was calculated based on a burned area-based approach. We
186   integrated different remotely sensed datasets that map regions affected by wildfires
187   and detect active fire spots to reconstruct the burned area. From 2012 to 2022, the
188   total burned area in China amounted to 5.31 ± 1.70 million hectares per year (Mha yr^{-1})
189   (Fig. 1). More than four-fifths of the total burned area were located in croplands,
190   equivalent to the land area of Switzerland. 11.0% of the burned area occurred in
191   various types of forests, while less than 6% of the burned area took place in grasslands
192   or other herbaceous-dominated regions. Based on this burned area estimates and
193   calculation of other components (emission factors, fuel loads, etc. see methods), our
194   results showed that annual wildfire-induced GHG emissions in China amounted to
195   78.13 ± 22.46 Tg CO_2, 279.47 ± 82.01 Gg CH_4, and 6.26 ± 1.67 Gigagrams (Gg) N_2O
196   (Fig. 1). Although the majority of all wildfire-induced GHG emissions were still caused
197   by cropland fires, the proportions were quite different from that in burned area. A fifth
198   of CO_2 (21.1%) and CH_4 (19.9%) emissions were caused by forest fires, which was
199   almost double than the contribution of this type measured in area. This comes from the
200   differences in background fuel loads as measured in carbon pools between forests and
201   cropland, reported by research on China's terrestrial ecosystems (Tang et al., 2018).

202   An even more substantial proportion of national N_2O emissions came from forest fires,
203   reaching up to 37.1% of the total(Fig. 1). Wildfire-induced N_2O emissions are highly
204   dependent on the ratio of carbon to nitrogen in vegetation fuels, which was higher in
205   woody areas (Vernooij et al., 2021). In comparisons to wildfires on other land cover
206   types, grassland fires played a comparatively minor role in wildfire dynamics and
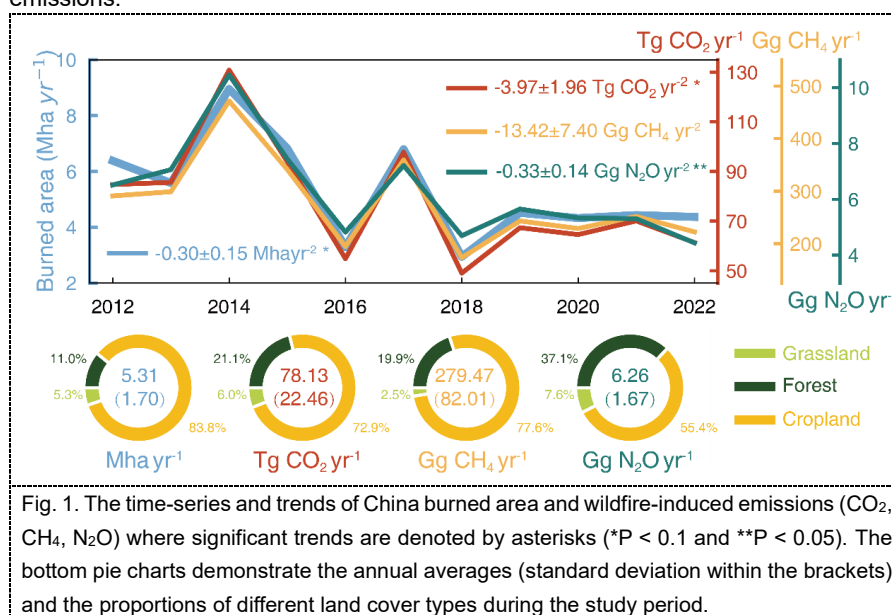207   emissions.

Fig. 1. The time-series and trends of China burned area and wildfire-induced emissions (CO_2, CH_4, N_2O) where significant trends are denoted by asterisks (*P < 0.1 and **P < 0.05). The bottom pie charts demonstrate the annual averages (standard deviation within the brackets) and the proportions of different land cover types during the study period.

208   During this period, the dataset recorded a decline trend of -0.31 ± 0.15 Mha yr^{-2}
209   (P<0.1) (Fig. 1). All vegetation wildfires decreased at different magnitudes, resulting in
210   pervasive and slightly different declines in the three greenhouse gases. Agricultural
211   fires had been gradually limited and demonstrated a decline in burned area at -0.26 ±
212   0.14 Mha yr^{-2}. Affected by the variations in cropland burned area, the three types of
213   GHGs in our dataset had a non-significant decline at -2.41 ± 1.81 Tg CO_2 yr^{-2}, -8.97 ±
214   6.96 Gg CH_4 yr^{-2} and -0.15 ± 0.11 Gg N_2O yr^{-2} during the study period. Compared with
215   cropland, burned area and all three types of wildfire-induced greenhouse gases in
216   forests and grasslands dropped significantly and rapidly. The decline in forest fires
217   contributed to nearly a third (CO_2 at -1.22 ± 0.36 Tg yr^{-2}, P<0.01 and CH_4 at -3.93 ±
218   1.21 Gg yr^{-2}, P<0.05) and a half (N_2O at -0.15 ± 0.05 Gg yr^{-2}, P<0.05) in the total trends
219   of emissions (Fig. S1). The grassland contributed smaller in all these GHGs (CO_2 at -
220   0.34 ± 0.08 Tg yr^{-2}, P<0.01, CH_4 at -0.51 ± 0.13 Gg yr^{-2}, P<0.01, and N_2O at -0.03 ±
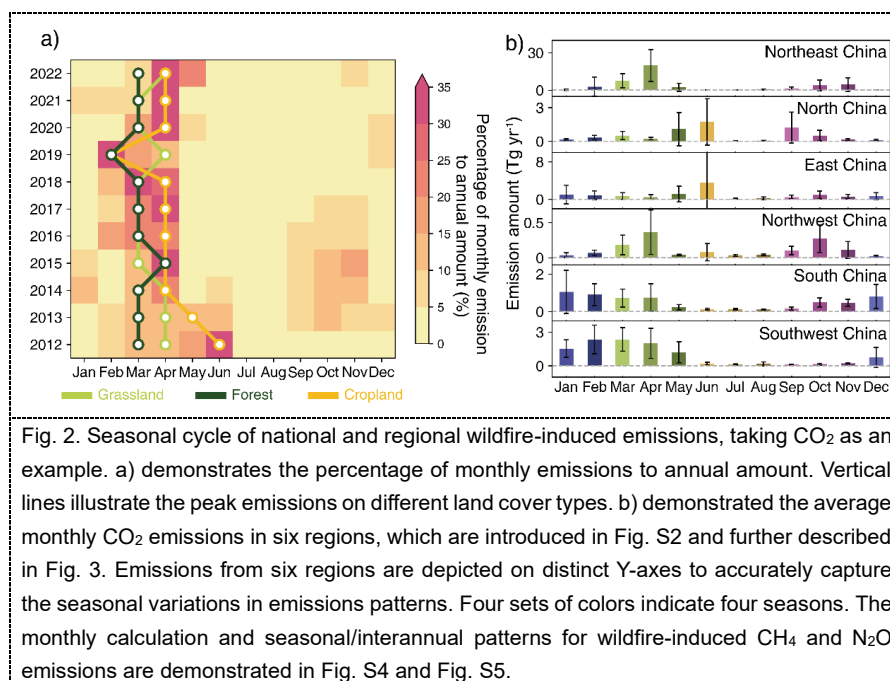221   0.01 Gg yr^{-2}, P<0.01) within the past decade.

Fig. 2. Seasonal cycle of national and regional wildfire-induced emissions, taking CO_2 as an example. a) demonstrates the percentage of monthly emissions to annual amount. Vertical lines illustrate the peak emissions on different land cover types. b) demonstrated the average monthly CO_2 emissions in six regions, which are introduced in Fig. S2 and further described in Fig. 3. Emissions from six regions are depicted on distinct Y-axes to accurately capture the seasonal variations in emissions patterns. Four sets of colors indicate four seasons. The monthly calculation and seasonal/interannual patterns for wildfire-induced CH_4 and N_2O emissions are demonstrated in Fig. S4 and Fig. S5.

222   The outcomes derived from diverse regions and land cover types underscored
223 those fires originating within cropland significantly dominated the overarching
224 dynamics of national wildfires and emissions. A spatiotemporal association was
225 assumed to exist between agricultural activities, particularly those related to planting
226 and harvesting preparations, and the incidence of wildfires. Throughout our study
227 period, the majority of all three types of GHG were concentrated in the first half of the
228 year. More than half of the annual CO_2 emissions from wildfires were observed from
229 late winter to middle spring (February to April), along with nearly the identical relative
230 proportions of CH_4 and N_2O. A secondary seasonal peak of wildfire-induced emissions
231 occurred in the harvest seasons in autumn (September to November), accounting for
232 nearly 20% of the annual total (Fig. 2a). We divided six specific wildfire-induced
233 emissions regions dependent on geographical location and environmental
234 characteristics (Fig. S2 and Table S3). The patterns of double peaks in agricultural fire
235 emissions in Northeast China had a significant impact on national emission levels.
236 During the major emission season, three quarters of the region's total annual amount
237 was emitted. It is important to note that the temporal patterns are closely associated
238 with the local sowing and harvesting seasons (Fig. 2b) (Cheng et al., 2022; WANG et
239 al., 2020). Similarly in North China, the major peak occurred in early summer (May and
240 June) while the secondary peak in mid-autumn (September and October). A total of
241 2.75 Tg and 1.65 Tg of annual CO_2 emissions induced by agricultural fires were
242 concentrated during these respective time periods. East China displayed disparate
243 seasonal patterns, with the majority of agricultural fires occurring during the summer
244 when the planting and harvest were made in double-season paddy rice fields in this
245 area (Fig. 2b) (Pan et al., 2021; Wu et al., 2023). Approximately one-third of the annual
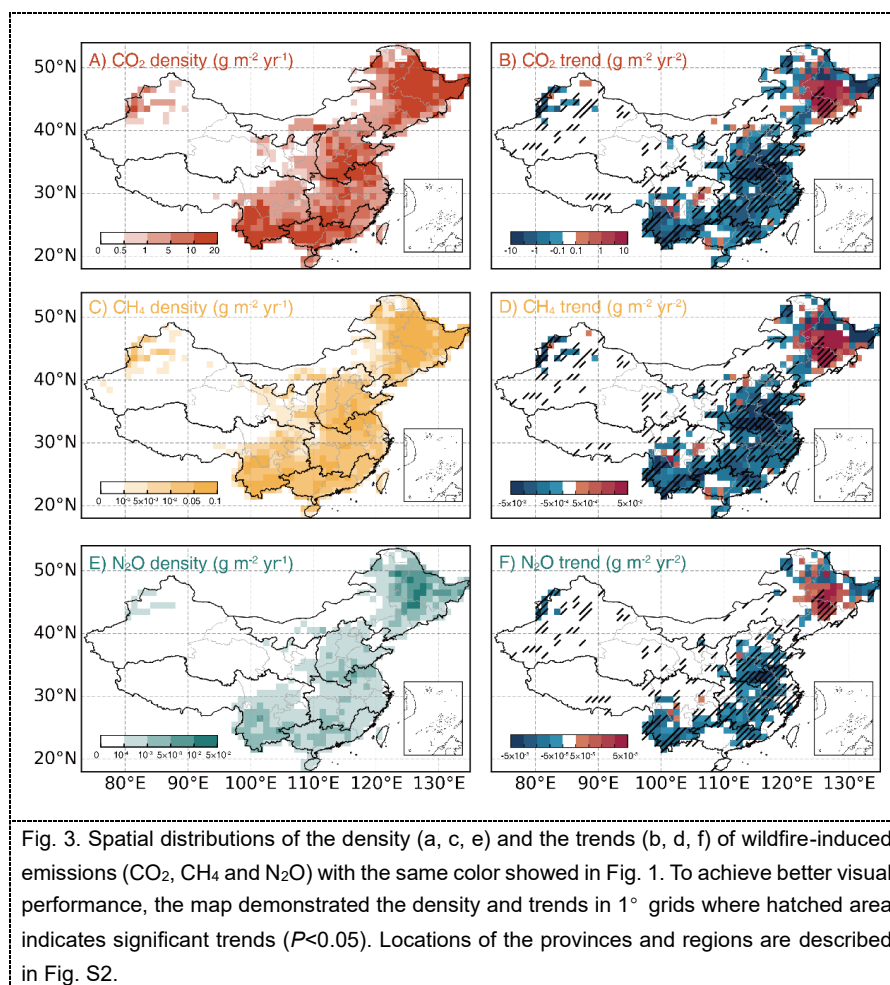
Geoscientific
Model Development
Discussions

246 regional emissions induced by wildfires were concentrated in June. Consequently, this
247 correlation is validated through the examination of seasonal cycles in wildfire
248 occurrences, which becomes a prominent temporal feature that drive the dynamics of
249 national-scale wildfire-induced emissions (Zhang et al., 2015).
250

251 **3.2 Spatiotemporal pattern of wildfire and its GHG emissions**

252 To further explore the fire emission dynamics, we calculated the provincial and
253 monthly burned areas and emissions, which were then aggregated to obtain regional
254 and seasonal statistics. The results showed that the national wildfire-induced
255 emissions shared similar patterns of all three GHG types in spite of their large
256 disparities at both spatial and temporal scales. More than four-fifths of the total of
257 domestic wildfire-induced GHG emissions (82.8% for CO_2, 83.2% for CH_4, and 83.6%
258 N_2O) located in three primary peaks, the Northeast, Southwest and East China,
259 respectively (Fig. 3), which will be introduced in detail in the upcoming sections.
260 In all six regions, Northeast China (Heilongjiang, Jilin, Liaoning and Nei Mongol)
261 affected by the highest wildfire emissions. Heilongjiang and Jilin were the top two
262 provinces not only within the region but also nationwide. Many of the burned area and
263 emissions located in vast plains (SongNen, Liaohe and Sanjiang plain) of Northeast
264 China. The vegetation-sourced fire emissions from these two provinces contributed to
265 nearly one-third and one-tenth of the total domestic emissions, individually. Moreover,
266 they exhibited a mild increasing trend compared to the national pattern, registering at
267 non-significant trends of 0.14 ± 0.15 Mha yr^{-2} for burned area and 1.92 ± 1.92 Tg yr^{-2},
268 6.94 ± 7.34 Gg yr^{-2} and 0.11 ± 0.13 Gg yr^{-2} for CO_2, CH_4 and N_2O, respectively (Fig. 4).
269 According to results from the National Bureau of Statistics, the total of these four
270 provinces contributed a quarter in sown area and grain production for the past decade.
271 The extensive grain acreage and prevailing practices of burning crop straws for land
272 clearance jointly contributed to the high wildfire-induced emissions in agricultural land
273 uses in Northeast China. CO_2 emissions from crop residue burning accounted for 82.7%
274 of the regional total wildfire-induced emissions and 62.5% of the domestic emissions
275 for this type. The rising trends of agricultural fires constitute the majority of regional
276 wildfire dynamics.
277 Fires have been controlled to an average of 0.27 Mha of burned area per year
278 through systematic fire and forest management in this area (Fig. 3 and Fig. 4). For
279 comparison, a single fire event, namely the 1987 Great Black Dragon Fire, destroyed
280 1.33 Mha of forests and resulted in nearly two hundred fatalities (Zhao et al., 2020;
281 Zong et al., 2022). The boreal forest wildfires led to 5.28 Tg CO_2, 19.44 Gg CH_4 and
282 0.94 Gg N_2O, constituting 12.3% of the total wildfire-induced emissions of this region.
283 This amount was also equivalent for nearly ninety percent of the boreal forest wildfire
284 emissions nationwide. Grassland fires in Northeast China, specifically in the Hulun Buir
285 and Xilingol grasslands, attracted national attention, accounting significantly for the
286 total amount at 67.2% for burned area and 46.7% for wildfire-induced emissions
287 respectively.

Fig. 3. Spatial distributions of the density (a, c, e) and the trends (b, d, f) of wildfire-induced emissions (CO_2, CH_4 and N_2O) with the same color showed in Fig. 1. To achieve better visual performance, the map demonstrated the density and trends in 1° grids where hatched area indicates significant trends ($P<0.05$). Locations of the provinces and regions are described in Fig. S2.

288   Southwest China, covering five provincial administrative areas (Yunnan, Sichuan
289 and Guizhou provinces, Chongqing and Xizang Autonomous Region), was the second-
290 largest regional scale emitter of fire-sourced greenhouse gases (Fig. 3). This region
291 stands out as the only area where agricultural wildfires do not dominate; instead,
292 temperate forest fires emitted more than all the other vegetation fires in this region (Fig.
293 4). Yunnan province, a pivotal player in shaping the wildfire dynamics of this region,
294 contributed substantially, with an annual burned area of 0.16 Mha, emitting 7.57 Tg
295 CO_2, 23.13 Gg CH_4, and 0.81 Gg N_2O (Cui et al., 2022; Ying et al., 2021). These figures
296 accounted for over 60% of the regional burned area and wildfire-induced emissions.
297 From the perspective of recent trends, this province contributed to 82.4% of the
298 regional decrease in burned area and even larger share in the reduction of wildfire-
299 induced emissions. The border fires showed some shared similarities in fire spreading
300 mechanisms and environmental factors between this region and the adjoining Indo-
301 China Peninsula, a global wildfire hotspot. However, in comparison to the rapid land
302 cover changes and massive relevant wildfires reported in Southeast Asian countries,

303 involving activities such as slash-and-burn, commercial forest loss, and drainage in
304 peatlands (Curtis et al., 2018; Page et al., 2022), Southwest China had fewer and
305 weaker fire activities related with this type. The occurrences of forest fires usually arose
306 from occasional personal activities or fire-related cultural traditions (Ying et al., 2021).
307 On the other hand, due to recent implementations of fire policies and long-standing
308 efforts from firefighting teams, Southwest China has experienced a significant decline
309 in forest fires, with a decrease of -0.02 ± 0.00 Mha yr^{-2} (P<0.01) for burned area and -
310 0.74 ± 0.23 Tg yr^{-2} (P<0.05), -2.38 ± 0.74 Gg yr^{-2} (P<0.05) and 0.09 ± 0.02 Gg yr^{-2}
311 (P<0.05) for CO_2, CH_4 and N_2O, respectively. This reduction accounts for more than
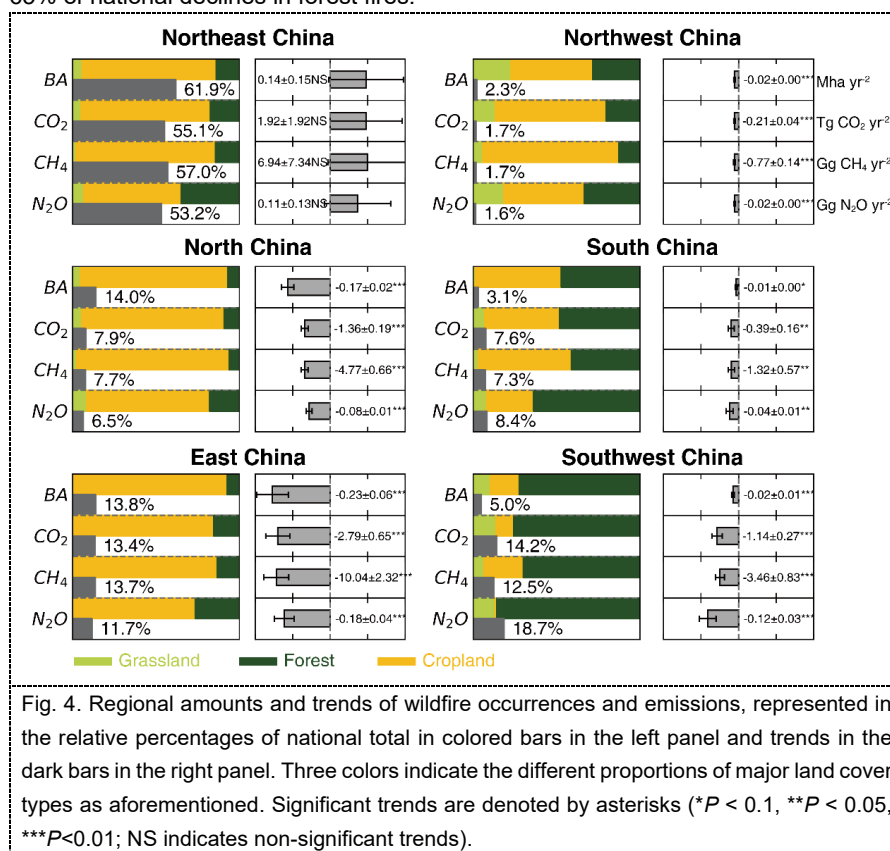312 65% of national declines in forest fires.

Fig. 4. Regional amounts and trends of wildfire occurrences and emissions, represented in the relative percentages of national total in colored bars in the left panel and trends in the dark bars in the right panel. Three colors indicate the different proportions of major land cover types as aforementioned. Significant trends are denoted by asterisks (*P < 0.1, **P < 0.05, ***P<0.01; NS indicates non-significant trends).

313 East China is another peak region of fire activities both in terms of burned area
314 and wildfire-induced emissions in our study. This region contains six provinces or
315 municipalities: Anhui, Jiangsu, Zhejiang, Hunan, Hubei and Shanghai where more than
316 70% CO_2 wildfire emissions came from crop residue burning except for Zhejiang
317 province. Similar to North China (Hebei, Henan, Shandong, Beijing and Tianjin),
318 wildfire patterns in East China are featured by high intensity in agricultural-sourced fire
319 emissions, with a total amount of more than 10 Tg wildfire emitted CO_2 and especially
320 concentrated in the Huanghuai Plain, namely the connection area of Shandong, Henan,
321 Jiangsu and Anhui. Altogether, these two regions have a half of the national sown area

322 and grain production and account for 30.8% in cropland burned area, 25.4% in wildfire-
323 induced CO_2 emissions (Fig. 4). During our study period, both of these two regions had
324 significant declines in agricultural fires at more than -0.22 ± 0.06 Mha yr^{-2} ($P<0.01$) and
325 -0.17 ± 0.02 Mha yr^{-2} ($P<0.01$) for East and North China, respectively. The decreasing
326 burned area in cropland led to -2.52 ± 0.64 Tg CO_2 yr^{-2} ($P<0.01$), -9.17 ± 2.28 Gg CH_4
327 yr^{-2} ($P<0.01$) and 0.15 ± 0.04 Gg N_2O yr^{-2} ($P<0.01$) in East China. By contrast, there
328 were an average of 0.59 Mha yr^{-1} in forest fires in the East China, three times higher
329 than that in North China. This further contributed to significantly more wildfire-induced
330 emission reduction, reaching 1.57 Tg CO_2, 5.03 Gg CH_4 and 0.19 Gg N_2O per year.
331

332 **3.3 Comparison with other results**

333   To assess the outcomes of this dataset, we conducted a comparative analysis by
334 juxtaposing our estimations with those from different studies or products. Our overall
335 emissions estimates demonstrate moderate values where the amount attributed to
336 agricultural fires was notably lower compared to former estimates. On average, the
337 quantities reported in regional to national scale studies were at least three times higher
338 than our results (Hong et al., 2023; Li et al., 2022; Wu et al., 2018). These studies
339 employed CYBA as aforementioned that the estimates of burned crop residues is
340 calculated by the multiplying the crop production derived from statistical data, the grain-
341 to-straw ratio from field-based analysis, and the proportion of crop residues burned in
342 the field using empirical summaries. Previous studies had found that the use of very
343 high residue burning ratios could be the reason for overestimates when compared with
344 results based on categorized cropland maps (Zhang et al., 2020). Directly utilizing
345 active fire pixels as proxies for the effects of fire activities can lead to higher values,
346 thereby contributing to an increase in emission estimates. To address this, we
347 employed an advanced satellite active fire dataset as a crucial supplementary
348 observation. This dataset allowed us to refine burned area estimates by reconstructing
349 external burned regions outside the original burned area data. We achieved this by
350 using circular kernels centered at active fire records, aligning with the national wildfire
351 dynamics, which are dominated by agricultural or small-sized fires. Two independent
352 active fire products and MCD64 burned area product were incorporated as baseline to
353 make intercomparison (Fig. 5). The sum of pixel area from MOD14 and VIIRS S-NPP
354 active fire products was translated to 6.77 ± 1.60 Mha and 8.20 ± 2.07 Mha per year
355 (Giglio et al., 2018, p.6; Schroeder et al., 2014). As a result, the burned area calculation
356 by directly counting all active fire pixels was at least 27.5% higher than our results.
357   Expanding to a broader scope, various global fire emission inventories have been
358 developed using different model settings. We selected four widely used products: (1)
359 Global Fire Emissions Database (GFED version 4.1s with small fire boosting) (van der
360 Werf et al., 2017), (2) Fire Inventory from NCAR (FINN version 2.5) (Wiedinmyer et al.,
361 2023), (3) Global Fire Assimilation System (GFAS version 1.2) (Kaiser et al., 2012) and
362 (4) Quick Fire Emissions Dataset (QFED version 2.5) (Koster et al., 2015). They
363 employ either burned area-based approaches (GFED and FINN) or fire energy-based
364 approaches (QFED and GFAS). Our results maintain similar ranges with other global
365 products (Fig. 5). The refined calculation for burned area estimates yielded higher

366 values than the sole use of burned area products and lower values than those only
367 consisting of active fire products (see details in Methods). Correspondingly, the GHGs
368 emissions were different as well when active fire-dominated product FINN had higher
369 estimates than ours. GFED demonstrated 64.3% to 90.3% of the results from
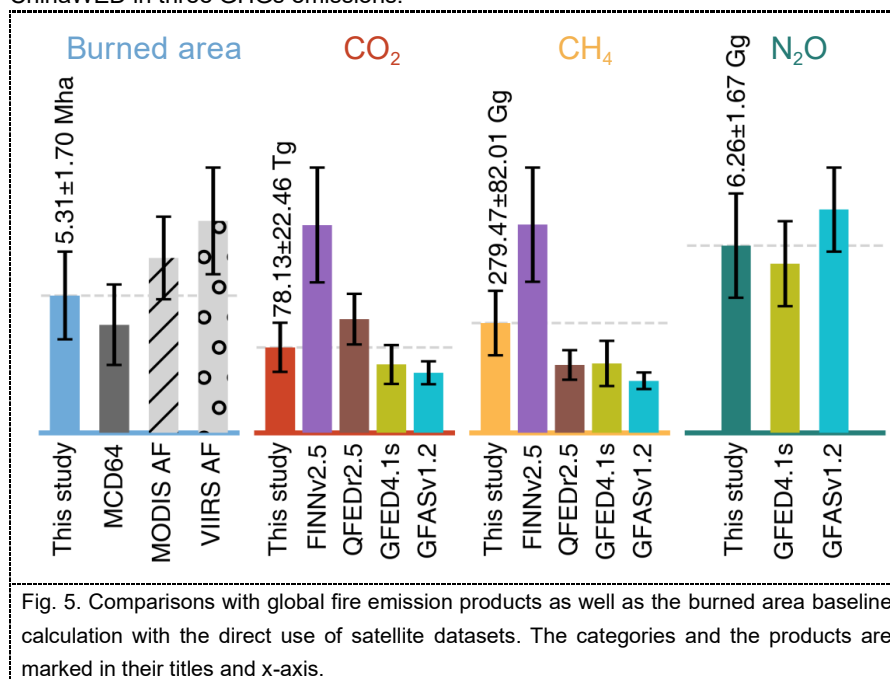370 ChinaWED in three GHGs emissions.

Fig. 5. Comparisons with global fire emission products as well as the burned area baseline calculation with the direct use of satellite datasets. The categories and the products are marked in their titles and x-axis.

371

4. Discussions

4.1 Influencing factors of the changes in wildfire seasonal cycles

374   In China, regulations and policies substantially impact anthropogenic activities
375 and thus the spatiotemporal distribution of the occurrences of wildfires and emissions.
376 In agricultural department, the policies have addressed on the issues of straw burning
377 due to its extensive aerosols and greenhouse gases emissions. In the early 21st
378 century, a specific law for prevention of air pollution was published, followed by the
379 releases of regulations on comprehensive utilization of straw (Wu et al., 2018; Zhang
380 et al., 2015). The national-scale "Air Pollution Prevention and Control Action Plan" was
381 initiated in 2013, with regional amendment progressively pushing from "legitimate
382 burning" policy to "strict prohibition" (Geng et al., 2021). Ground-based studies and
383 satellite-based estimations have documented a rapid decrease in burned area and
384 emissions across significant regions of the country. Another consequential effect of the
385 implementation of these banning policies has been the shifts in burning seasons (Ding
386 et al., 2019; Zhang et al., 2020). Despite Northeast China being the only region with
387 trends contrary to the national declines, a shift in the primary burning season from
388 autumn to spring was also observed in this area after 2013 due to the implementation

389   of straw burning bans (Cheng et al., 2022; WANG et al., 2020).

390   It has been reported that there has been a noticeable decline in the global burned
391   area driven by the expansion and intensified capital management in agricultural land
392   use (Andela et al., 2017). Since the beginning of the 21st century, there has also been
393   a growing emphasis on fire management within both administrative bodies and
394   scientific communities in China. This evolution has contributed to a more stringent
395   implementation, particularly in controlling ignition sources in agricultural practices and
396   forest and grassland areas. From local fire suppression measures to national ignition-
397   proof initiatives, efforts have been progressively employed to bring forest fires under
398   control (Chen et al., 2019; Ying et al., 2018). In comparison with forest fire dynamics
399   reported in previous studies focusing on the first decade of this century, the southern
400   part of China experienced a significant decline in burned area as well as wildfire-
401   induced emissions (Wang et al., 2023b; Ying et al., 2018; Zong et al., 2022). Whilst the
402   establishment and improvement of legal systems and infrastructure for forest and
403   grassland fire prevention, dealing with uncontrolled transboundary fires remains
404   challenging. Nationally, an area of 0.07 Mha yr^{-1} was affected within the 10 km buffer
405   zone near the borders with neighboring countries. This accounted for 1.3% of domestic
406   burned area and contributed to 1.03 Tg yr^{-1} of CO_2, 3.35 Gg yr^{-1} of CH_4, and 0.09 Gg
407   yr^{-1} of N_2O.

408

409   4.2 Improvements of ChinaWED to previous studies

410   As described in the aforementioned texts, we refined our estimates of emission
411   factors, fuel loadings and burned area mainly with a set of more localized parameters
412   and advanced satellite-based observations. Fuel loadings in these previous global
413   products are mainly derived from biogeochemical models in these global products.
414   According to the recent studies, the use of aboveground biomass (AGB) as a proxy of
415   fuel loadings can enable indirect estimations of dry matter and improve fire emission
416   estimates (Di Giuseppe et al., 2021). We thus used a high-resolution harmonized
417   carbon density map that was consistently and seamlessly reported across a wide
418   range of vegetation types based on the relative spatial extent of each type. Emission
419   factor is a scalar that evaluate the ratio between emission and the total amount of dry
420   matter that was consumed during burning processes. In this study in addition to the
421   previously summarized emission factors, we collected the field-based research in
422   China and neighboring countries and recompiled the values into the new table of
423   wildfire emission factors for different land cover types. The detailed selection of these
424   components can be found in Table S2.

425   Additionally in the estimates of burned area, ChinaWED leveraged the sensitivity
426   of active fire products with higher spatial resolution and developed a new set of
427   calculation method that were suitable for smaller fires. The global products had
428   different frameworks where FINN focuses on active fire detection clusters joined for
429   the determination of extended burned areas and the burned area from GFED is mainly
430   derived based on a linear combination of the distribution of active fire and original
431   burned area data. QFED and GFAS utilize fire energy as the intermediate product to
432   represent the effects of fires for estimating wildfire-induced emissions. These models

433 employ empirical continuous functions to incorporate discrete observations and
434 calculate the temporal integral of fire radiative power (FRP). Furthermore, ChinaWED
435 is designed for the analysis of wildfire-induced GHG emissions. Most products reported
436 wildfire-induced CO_2 and CH_4 emissions while only two of them provided N_2O emission
437 estimates (Fig. 5).
438

Code and data availability

440 Python code for this model can be obtained from https://zenodo.org/records/13800556
441 (python version 3.11.6). Key packages used in the code include rasterio (version 1.3.9),
442 numpy (version 1.25.2), pandas (version 2.1.3) and scipy (version 1.10.1). Fire
443 products include MCD64A1.061 (doi.org/10.5067/MODIS/MCD64A1.061) and VIIRS
444 S-NPP active fire (doi.org/10.1016/j.rse.2013.12.008). Aboveground biomass data is
445 available from doi.org/10.1038/s41597-020-0444-4. Different crop types are available
446 from double season paddy rice (doi.org/10.3390/rs13224609), single season rice
447 (doi.org/10.57760/sciencedb.06963), maize (doi:10.6084/m9.figshare.17091653),
448 winter wheat (doi.org/10.6084/m9.figshare.12003990) and sugarcane
449 (doi.org/10.3390/rs14051274), respectively.
450

5. Conclusions

452 Wildfire is one of the most common land-surface disturbances to ecological and
453 socioeconomical processes. It combusts vegetation and releases greenhouse gases
454 and aerosols. Employing the burned area-based approach, we featured multisource
455 fire locations, updated emission factors, and high-resolution fuel load maps to generate
456 a new China wildfire emission dataset. The wildfire dynamics showed that during the
457 past decade, an average of 5.31 ± 1.70 Mha burned area, 78.13 ± 22.46 Tg CO_2,
458 279.47 ± 82.01 Gg CH_4, and 6.26 ± 1.67 Gg N_2O per year was observed. At the national
459 scale, the spatiotemporal characteristics of fire occurrences were markedly influenced
460 by agricultural activities, which contributed to more than four-fifths in area and at least
461 half in greenhouse gas emissions. The extensive agricultural fires played an important
462 role in shaping the seasonal cycle of wildfire emissions (Hong et al., 2023; Xu et al.,
463 2023). Northeast, North, and East China emerged as hotspots for this type of fires,
464 with the major peak of emissions occurring in mid-spring to early-summer. We
465 observed rapid and significant decline of burned area and wildfire-induced emissions
466 in vast areas in China that may be largely attributed to the implementation of fire
467 prevention and bans on straw burning. Notably, the relative decline rate of burned,
468 translating to around 5.8% per year, was four times higher than the global average
469 (Andela et al., 2017). Northeast China was the only region with an opposite trend,
470 suggesting a situation that requires more adaptive policies rather than mandatory bans.
471 Compared with estimations by other studies and global products, our results have
472 moderate values where the mismatches in burned area and estimates of burned crop
473 residues contributed largely. Overall, the calculation of burned area for small-sized fire
474 activities and the recalibrated emission factors, tailored for wildfires in China, contribute

475 to the findings of this study. These results offer new insights into the spatiotemporal
476 patterns of China's wildfire-induced greenhouse gas emissions and provide important
477 estimates as a part of the budget for the national terrestrial ecosystems. Future
478 updates will focus on integrating additional field-based studies and refining the
479 estimates of various burning processes.
480
481

Author contribution

483   X.W. designed the study. Z.L. developed the model code and performed the
484 analyses. Z.L., L.H. and X.W. interpreted the results. Z.L. and H.L. prepared the first
485 version of the manuscript with contributions from all co-authors.
486

Competing interests

488   The authors declared that none of the authors has any competing interest
489
490
491
492
493
494

Reference

495

496 Andela, N., Morton, D. C., Giglio, L., Chen, Y., van der Werf, G. R., Kasibhatla, P.
497 S., DeFries, R. S., Collatz, G. J., Hantson, S., Kloster, S., Bachelet, D., Forrest, M.,
498 Lasslop, G., Li, F., Mangeon, S., Melton, J. R., Yue, C., and Randerson, J. T.: A human-
499 driven decline in global burned area, Science, 356, 1356–1362,
500 https://doi.org/10.1126/science.aal4108, 2017.

501 Bauters, M., Drake, T. W., Wagner, S., Baumgartner, S., Makelele, I. A., Bode, S.,
502 Verheyen, K., Verbeeck, H., Ewango, C., Cizungu, L., Van Oost, K., and Boeckx, P.:
503 Fire-derived phosphorus fertilization of African tropical forests, Nature
504 Communications, 12, 5129, https://doi.org/10.1038/s41467-021-25428-3, 2021.

505 Beck, H. E., Zimmermann, N. E., McVicar, T. R., Vergopolan, N., Berg, A., and
506 Wood, E. F.: Present and future Köppen-Geiger climate classification maps at 1-km
507 resolution, Scientific Data, 5, 180214, https://doi.org/10.1038/sdata.2018.214, 2018.

508 Chen, A., Tang, R., Mao, J., Yue, C., Li, X., Gao, M., Shi, X., Jin, M., Ricciuto, D.,
509 Rabin, S., Ciais, P., and Piao, S.: Spatiotemporal dynamics of ecosystem fires and
510 biomass burning-induced carbon emissions in China over the past two decades,
511 Geography and Sustainability, 1, 47–58, https://doi.org/10.1016/j.geosus.2020.03.002,
512 2020.

513 Chen, C., Park, T., Wang, X., Piao, S., Xu, B., Chaturvedi, R. K., Fuchs, R., Brovkin,
514 V., Ciais, P., Fensholt, R., Tommervik, H., Bala, G., Zhu, Z., Nemani, R. R., and Myneni,
515 R. B.: China and India lead in greening of the world through land-use management,
516 Nature Sustainability, 2, 122–129, https://doi.org/10.1038/s41893-019-0220-7, 2019.

517 Cheng, Y., Cao, X., Liu, J., Yu, Q., Zhong, Y., Geng, G., Zhang, Q., and He, K.:
518 New open burning policy reshaped the aerosol characteristics of agricultural fire
519 episodes in Northeast China, Science of The Total Environment, 810, 152272,
520 https://doi.org/10.1016/j.scitotenv.2021.152272, 2022.

521 Cui, L., Luo, C., Yao, C., Zou, Z., Wu, G., Li, Q., and Wang, X.: The Influence of
522 Climate Change on Forest Fires in Yunnan Province, Southwest China Detected by
523 GRACE Satellites, Remote Sensing, 14, 712, https://doi.org/10.3390/rs14030712,
524 2022.

525 Curtis, P. G., Slay, C. M., Harris, N. L., Tyukavina, A., and Hansen, M. C.:
526 Classifying drivers of global forest loss, Science, 361, 1108–1111,
527 https://doi.org/10.1126/science.aau3445, 2018.

528 Di Giuseppe, F., Benedetti, A., Coughlan, R., Vitolo, C., and Vuckovic, M.: A Global
529 Bottom-Up Approach to Estimate Fuel Consumed by Fires Using Above Ground
530 Biomass Observations, Geophys. Res. Lett., 48, e2021GL095452,
531 https://doi.org/10.1029/2021gl095452, 2021.

532   Ding, A., Huang, X., Nie, W., Chi, X., Xu, Z., Zheng, L., Xu, Z., Xie, Y., Qi, X., Shen,
533   Y., Sun, P., Wang, J., Wang, L., Sun, J., Yang, X.-Q., Qin, W., Zhang, X., Cheng, W.,
534   Liu, W., Pan, L., and Fu, C.: Significant reduction of PM2.5 in eastern china due to
535   regional-scale emission control: evidence from SORPES in 2011–2018, Atmospheric
536   Chemistry and Physics, 19, 11791–11801, https://doi.org/10.5194/acp-19-11791-2019,
537   2019.

538   Dong, J., Fu, Y., Wang, J., Tian, H., Fu, S., Niu, Z., Han, W., Zheng, Y., Huang, J.,
539   and Yuan, W.: Early-season mapping of winter wheat in China based on Landsat and
540   Sentinel images, Earth Syst. Sci. Data, 12, 3081–3095, https://doi.org/10.5194/essd-
541   12-3081-2020, 2020.

542   Friedlingstein, P., O'Sullivan, M., Jones, M. W., Andrew, R. M., Gregor, L., Hauck,
543   J., Le Quéré, C., Luijkx, I. T., Olsen, A., Peters, G. P., Peters, W., Pongratz, J.,
544   Schwingshackl, C., Sitch, S., Canadell, J. G., Ciais, P., Jackson, R. B., Alin, S. R.,
545   Alkama, R., Arneth, A., Arora, V. K., Bates, N. R., Becker, M., Bellouin, N., Bittig, H. C.,
546   Bopp, L., Chevallier, F., Chini, L. P., Cronin, M., Evans, W., Falk, S., Feely, R. A.,
547   Gasser, T., Gehlen, M., Gkritzalis, T., Gloege, L., Grassi, G., Gruber, N., Gürses, Ö.,
548   Harris, I., Hefner, M., Houghton, R. A., Hurtt, G. C., Iida, Y., Ilyina, T., Jain, A. K., Jersild,
549   A., Kadono, K., Kato, E., Kennedy, D., Klein Goldewijk, K., Knauer, J., Korsbakken, J.
550   I., Landschützer, P., Lefèvre, N., Lindsay, K., Liu, J., Liu, Z., Marland, G., Mayot, N.,
551   McGrath, M. J., Metzl, N., Monacci, N. M., Munro, D. R., Nakaoka, S.-I., Niwa, Y.,
552   O'Brien, K., Ono, T., Palmer, P. I., Pan, N., Pierrot, D., Pocock, K., Poulter, B.,
553   Resplandy, L., Robertson, E., Rödenbeck, C., Rodriguez, C., Rosan, T. M., Schwinger,
554   J., Séférian, R., Shutler, J. D., Skjelvan, I., Steinhoff, T., Sun, Q., Sutton, A. J., Sweeney,
555   C., Takao, S., Tanhua, T., Tans, P. P., Tian, X., Tian, H., Tilbrook, B., Tsujino, H., Tubiello,
556   F., van der Werf, G. R., Walker, A. P., Wanninkhof, R., Whitehead, C., Willstrand
557   Wranne, A., et al.: Global Carbon Budget 2022, Earth System Science Data, 14, 4811–
558   4900, https://doi.org/10.5194/essd-14-4811-2022, 2022.

559   Geng, G., Zheng, Y., Zhang, Q., Xue, T., Zhao, H., Tong, D., Zheng, B., Li, M., Liu,
560   F., Hong, C., He, K., and Davis, S. J.: Drivers of PM2.5 air pollution deaths in China
561   2002–2017, Nature Geoscience, 14, 645–650, https://doi.org/10.1038/s41561-021-
562   00792-3, 2021.

563   Giglio, L., Boschetti, L., Roy, D. P., Humber, M. L., and Justice, C. O.: The
564   Collection 6 MODIS burned area mapping algorithm and product, Remote Sensing of
565   Environment, 217, 72–85, https://doi.org/10.1016/j.rse.2018.08.005, 2018.

566   Guo, J., Feng, H., Peng, C., Du, J., Wang, W., Kneeshaw, D., Pan, C., Roberge,
567   G., Feng, L., and Chen, A.: Fire effects on soil CH4 and N2O fluxes across terrestrial
568   ecosystems, Science of The Total Environment, 948, 174708,
569   https://doi.org/10.1016/j.scitotenv.2024.174708, 2024.

570   Hong, X., Zhang, C., Tian, Y., Wu, H., Zhu, Y., and Liu, C.: Quantification and
571   evaluation of atmospheric emissions from crop residue burning constrained by satellite

Geoscientific
Model Development
Discussions

572   observations in China during 2016–2020, Science of The Total Environment, 865,
573   161237, https://doi.org/10.1016/j.scitotenv.2022.161237, 2023.

574   Kaiser, J. W., Heil, A., Andreae, M. O., Benedetti, A., Chubarova, N., Jones, L.,
575   Morcrette, J. J., Razinger, M., Schultz, M. G., Suttie, M., and van der Werf, G. R.:
576   Biomass burning emissions estimated with a global fire assimilation system based on
577   observed fire radiative power, Biogeosciences, 9, 527–554, https://doi.org/10.5194/bg-
578   9-527-2012, 2012.

579   Koster, R. D., Darmenov, A. S., and da Silva, A. M.: The Quick Fire Emissions
580   Dataset (QFED): Documentation of Versions 2.1, 2.2 and 2.4, 2015.

581   Li, J., Li, Y., Bo, Y., and Xie, S.: High-resolution historical emission inventories of
582   crop residue burning in fields in China for the period 1990–2013, Atmospheric
583   Environment, 138, 152–161, https://doi.org/10.1016/j.atmosenv.2016.05.002, 2016.

584   Li, R., He, X., Wang, H., Wang, Y., Zhang, M., Mei, X., Zhang, F., and Chen, L.:
585   Estimating Emissions from Crop Residue Open Burning in Central China from 2012 to
586   2020 Using Statistical Models Combined with Satellite Observations, Remote Sensing,
587   14, 3682, https://doi.org/10.3390/rs14153682, 2022.

588   Li, W., MacBean, N., Ciais, P., Defourny, P., Lamarche, C., Bontemps, S.,
589   Houghton, R. A., and Peng, S.: Gross and net land cover changes in the main plant
590   functional types derived from the annual ESA CCI land cover maps (1992–2015), Earth
591   System Science Data, 10, 219–234, https://doi.org/10.5194/essd-10-219-2018, 2018.

592   Liu, Y., Hu, C., Zhan, W., Sun, C., Murch, B., and Ma, L.: Identifying industrial heat
593   sources using time-series of the VIIRS Nightfire product with an object-oriented
594   approach, Remote Sensing of Environment, 204, 347–365,
595   https://doi.org/10.1016/j.rse.2017.10.019, 2018.

596   Liu, Z., Deng, Z., He, G., Wang, H., Zhang, X., Lin, J., Qi, Y., and Liang, X.:
597   Challenges and opportunities for carbon neutrality in China, Nat Rev Earth Environ, 3,
598   141–155, https://doi.org/10.1038/s43017-021-00244-x, 2022.

599   Noon, M. L., Goldstein, A., Ledezma, J. C., Roehrdanz, P. R., Cook-Patton, S. C.,
600   Spawn-Lee, S. A., Wright, T. M., Gonzalez-Roglich, M., Hole, D. G., Rockström, J., and
601   Turner, W. R.: Mapping the irrecoverable carbon in Earth's ecosystems, Nature
602   Sustainability, 5, 37–46, https://doi.org/10.1038/s41893-021-00803-6, 2022.

603   Page, S., Mishra, S., Agus, F., Anshari, G., Dargie, G., Evers, S., Jauhiainen, J.,
604   Jaya, A., Jovani-Sancho, A. J., Laurén, A., Sjögersten, S., Suspense, I. A., Wijedasa,
605   L. S., and Evans, C. D.: Anthropogenic impacts on lowland tropical peatland
606   biogeochemistry, Nature Reviews Earth & Environment, 3, 426–443,
607   https://doi.org/10.1038/s43017-022-00289-6, 2022.

608   Pan, B., Zheng, Y., Shen, R., Ye, T., Zhao, W., Dong, J., Ma, H., and Yuan, W.:

609   High Resolution Distribution Dataset of Double-Season Paddy Rice in China, Remote
610   Sensing, 13, 4609, https://doi.org/10.3390/rs13224609, 2021.

611   Rodríguez Vásquez, M. J., Benoist, A., Roda, J.-M., and Fortin, M.: Estimating
612   Greenhouse Gas Emissions From Peat Combustion in Wildfires on Indonesian
613   Peatlands, and Their Uncertainty, Global Biogeochemical Cycles, 35,
614   e2019GB006218, https://doi.org/10.1029/2019GB006218, 2021.

615   Schroeder, W., Oliva, P., Giglio, L., and Csiszar, I. A.: The New VIIRS 375 m active
616   fire detection data product: Algorithm description and initial assessment, Remote
617   Sensing of Environment, 143, 85–96, https://doi.org/10.1016/j.rse.2013.12.008, 2014.

618   Shen, R., Dong, J., Yuan, W., Han, W., Ye, T., and Zhao, W.: A 30 m Resolution
619   Distribution Map of Maize for China Based on Landsat and Sentinel Images, Journal
620   of Remote Sensing, 2022, https://doi.org/10.34133/2022/9846712, 2022.

621   Shen, R., Pan, B., Peng, Q., Dong, J., Chen, X., Zhang, X., Ye, T., Huang, J., and
622   Yuan, W.: High-resolution distribution maps of single-season rice in China from 2017
623   to 2022, Earth Syst. Sci. Data, 15, 3203–3222, https://doi.org/10.5194/essd-15-3203-
624   2023, 2023.

625   Spawn, S. A., Sullivan, C. C., Lark, T. J., and Gibbs, H. K.: Harmonized global
626   maps of above and belowground biomass carbon density in the year 2010, Sci Data,
627   7, 112, https://doi.org/10.1038/s41597-020-0444-4, 2020.

628   Tang, X., Zhao, X., Bai, Y., Tang, Z., Wang, W., Zhao, Y., Wan, H., Xie, Z., Shi, X.,
629   Wu, B., Wang, G., Yan, J., Ma, K., Du, S., Li, S., Han, S., Ma, Y., Hu, H., He, N., Yang,
630   Y., Han, W., He, H., Yu, G., Fang, J., and Zhou, G.: Carbon pools in China's terrestrial
631   ecosystems: New estimates based on an intensive field survey, Proceedings of the
632   National Academy of Sciences, 115, 4021–4026,
633   https://doi.org/10.1073/pnas.1700291115, 2018.

634   Vernooij, R., Giongo, M., Borges, M. A., Costa, M. M., Barradas, A. C. S., and Van
635   Der Werf, G. R.: Intraseasonal variability of greenhouse gas emission factors from
636   biomass burning in the Brazilian Cerrado, Biogeosciences, 18, 1375–1393,
637   https://doi.org/10.5194/bg-18-1375-2021, 2021.

638   WANG, L., JIN, X., WANG, Q., MAO, H., LIU, Q., WENG, G., and WANG, Y.:
639   Spatial and temporal variability of open biomass burning in Northeast China from 2003
640   to 2017, Atmospheric and Oceanic Science Letters, 13, 240–247,
641   https://doi.org/10.1080/16742834.2020.1742574, 2020.

642   Wang, S., Zhang, H., Feng, Z., Wang, Y., Su, J., Gao, K., and Li, J.: Dispersal
643   Limitation Dominates the Spatial Distribution of Forest Fuel Loads in Chongqing, China,
644   Ecosystem Health and Sustainability, 9, 0079, https://doi.org/10.34133/ehs.0079,
645   2023a.

646   Wang, Z., Huang, R., Yao, Q., Zong, X., Tian, X., Zheng, B., and Trouet, V.: Strong
647   winds drive grassland fires in China, Environ. Res. Lett., 18, 015005,
648   https://doi.org/10.1088/1748-9326/aca921, 2023b.

649   van Wees, D., van der Werf, G. R., Randerson, J. T., Rogers, B. M., Chen, Y.,
650   Veraverbeke, S., Giglio, L., and Morton, D. C.: Global biomass burning fuel
651   consumption and emissions at 500 m spatial resolution based on the Global Fire
652   Emissions Database (GFED), Geoscientific Model Development, 15, 8411–8437,
653   https://doi.org/10.5194/gmd-15-8411-2022, 2022.

654   van der Werf, G. R., Randerson, J. T., Giglio, L., van Leeuwen, T. T., Chen, Y.,
655   Rogers, B. M., Mu, M., van Marle, M. J. E., Morton, D. C., Collatz, G. J., Yokelson, R.
656   J., and Kasibhatla, P. S.: Global fire emissions estimates during 1997-2016, Earth Syst.
657   Sci. Data, 9, 697–720, https://doi.org/10.5194/essd-9-697-2017, 2017.

658   Wiedinmyer, C., Kimura, Y., McDonald-Buller, E. C., Emmons, L. K., Buchholz, R.
659   R., Tang, W., Seto, K., Joseph, M. B., Barsanti, K. C., Carlton, A. G., and Yokelson, R.:
660   The Fire Inventory from NCAR version 2.5: an updated global fire emissions model for
661   climate   and   chemistry   applications,   EGUsphere,   1–45,
662   https://doi.org/10.5194/egusphere-2023-124, 2023.

663   Wu, H., Zhang, J., Zhang, Z., Han, J., Cao, J., Zhang, L., Luo, Y., Mei, Q., Xu, J.,
664   and Tao, F.: AsiaRiceYield4km: seasonal rice yield in Asia from 1995 to 2015, Earth
665   System Science Data, 15, 791–808, https://doi.org/10.5194/essd-15-791-2023, 2023.

666   Wu, J., Kong, S., Wu, F., Cheng, Y., Zheng, S., Yan, Q., Zheng, H., Yang, G.,
667   Zheng, M., Liu, D., Zhao, D., and Qi, S.: Estimating the open biomass burning
668   emissions in central and eastern China from 2003 to 2015 based on satellite
669   observation, Atmospheric Chemistry and Physics, 18, 11623–11646,
670   https://doi.org/10.5194/acp-18-11623-2018, 2018.

671   Xu, R., Ye, T., Yue, X., Yang, Z., Yu, W., Zhang, Y., Bell, M. L., Morawska, L., Yu,
672   P., Zhang, Y., Wu, Y., Liu, Y., Johnston, F., Lei, Y., Abramson, M. J., Guo, Y., and Li, S.:
673   Global population exposure to landscape fire air pollution from 2000 to 2019, Nature,
674   621, 521–529, https://doi.org/10.1038/s41586-023-06398-6, 2023.

675   Ying, L., Han, J., Du, Y., and Shen, Z.: Forest fire characteristics in China: Spatial
676   patterns and determinants with thresholds, Forest Ecology and Management, 424,
677   345–354, https://doi.org/10.1016/j.foreco.2018.05.020, 2018.

678   Ying, L., Cheng, H., Shen, Z., Guan, P., Luo, C., and Peng, X.: Relative humidity
679   and agricultural activities dominate wildfire ignitions in yunnan, southwest china:
680   patterns, thresholds, and implications, Agricultural and Forest Meteorology, 307,
681   108540, https://doi.org/10.1016/j.agrformet.2021.108540, 2021.

682   Zhang, H., Ye, X., Cheng, T., Chen, J., Yang, X., Wang, L., and Zhang, R.: A

683 laboratory study of agricultural crop residue combustion in china: emission factors and
684 emission inventory, Atmospheric Environment, 42, 8432–8441,
685 https://doi.org/10.1016/j.atmosenv.2008.08.015, 2008.

686 Zhang, H., Hu, D., Chen, J., Ye, X., Wang, S. X., Hao, J. M., Wang, L., Zhang, R.,
687 and An, Z.: Particle Size Distribution and Polycyclic Aromatic Hydrocarbons Emissions
688 from Agricultural Crop Residue Burning, Environmental Science & Technology, 45,
689 5477–5482, https://doi.org/10.1021/es1037904, 2011.

690 Zhang, T., Wooster, M. J., Green, D. C., and Main, B.: New field-based agricultural
691 biomass burning trace gas, PM2.5, and black carbon emission ratios and factors
692 measured in situ at crop residue fires in eastern china, Atmospheric Environment, 121,
693 22–34, https://doi.org/10.1016/j.atmosenv.2015.05.010, 2015.

694 Zhang, T., de Jong, M. C., Wooster, M. J., Xu, W., and Wang, L.: Trends in eastern
695 China agricultural fire emissions derived from a combination of geostationary
696 (Himawari) and polar (VIIRS) orbiter fire radiative power products, Atmospheric
697 Chemistry and Physics, 20, 10687–10705, https://doi.org/10.5194/acp-20-10687-2020,
698 2020.

699 Zhao, F., Liu, Y., and Shu, L.: Change in the fire season pattern from bimodal to
700 unimodal under climate change: The case of Daxing'anling in Northeast China,
701 Agricultural and Forest Meteorology, 291, 108075,
702 https://doi.org/10.1016/j.agrformet.2020.108075, 2020.

703 Zheng, Y., Li, Z., Pan, B., Lin, S., Dong, J., Li, X., and Yuan, W.: Development of
704 a Phenology-Based Method for Identifying Sugarcane Plantation Areas in China Using
705 High-Resolution Satellite Datasets, Remote Sensing, 14, 1274,
706 https://doi.org/10.3390/rs14051274, 2022.

707 Zong, X., Tian, X., Yao, Q., Brown, P. M., Zong, X., Tian, X., Yao, Q., and Brown,
708 P. M.: An analysis of fatalities from forest fires in China, 1951–2018, Int. J. Wildland
709 Fire, 31, 507–517, https://doi.org/10.1071/WF21137, 2022.

710
711